

Nonlinear dynamics in the Einstein-Gauss-Bonnet gravityHisaki Shinkai^{1,*} and Takashi Torii^{2,†}¹*Department of Information Systems, Faculty of Information Science & Technology,
Osaka Institute of Technology, Kitayama, Hirakata City, Osaka 573-0196, Japan*²*Department of System Design, Faculty of Robotics & Design, Osaka Institute of Technology,
Kita-ku, Osaka City, Osaka 530-8568, Japan*

(Received 7 June 2017; published 9 August 2017)

We numerically investigated how nonlinear dynamics depends on the dimensionality and on the higher-order curvature corrections in the form of Gauss-Bonnet (GB) terms. We especially monitored the processes of appearances of a singularity (or black hole) in two models: (i) a perturbed wormhole throat in spherically symmetric space-time, and (ii) colliding scalar pulses in plane-symmetric space-time. We used a dual-null formulation for evolving the field equations, which enables us to locate the trapping horizons directly, and also enables us to follow close to the large-curvature region due to its causal integrating scheme. We observed that the fate of a perturbed wormhole is either a black hole or an expanding throat depending on the total energy of the structure, and its threshold depends on the coupling constant of the GB terms (α_{GB}). We also observed that a collision of large scalar pulses will produce a large-curvature region, of which the magnitude also depends on α_{GB} . For both models, the normal corrections ($\alpha_{\text{GB}} > 0$) work for avoiding the appearance of singularity, although it is inevitable. We also found that in the critical situation for forming a black hole, the existence of the trapped region in the Einstein-GB gravity does not directly indicate the formation of a black hole.

DOI: [10.1103/PhysRevD.96.044009](https://doi.org/10.1103/PhysRevD.96.044009)**I. INTRODUCTION**

Nobody raises an objection to the fact that general relativity (GR) describes the nature of strong gravity quite well. The success of the standard big-bang theory is recognized as the most successful physical result in the 20th century, and black-hole physics is now applied to understand several field theories and/or material physics. We have also seen the first direct detection of gravitational waves, achieved a century after Einstein's theoretical discovery.

One of our most exciting topics now is what the physics laws beyond GR are. We know that GR cannot merge with quantum theory in its current form. We also know that standard cosmology still requires new ideas to explain the matter contents and the rate of expansion of space-time. There are several approaches to these problems. Among them, we think that gravity theories in higher-dimensional space-time and/or in the theories with higher-order curvature terms are the natural extensions to be considered.

We present in this article several nonlinear behaviors in gravity theory with the Gauss-Bonnet (GB) terms [1–3]. The Einstein-GB gravity is derived from string theory, with additional higher-order-curvature correction terms added to GR in the form of the Lagrangian

$$\mathcal{L}_{\text{GB}} = \mathcal{R}^2 - 4\mathcal{R}_{\mu\nu}\mathcal{R}^{\mu\nu} + \mathcal{R}_{\mu\nu\rho\sigma}\mathcal{R}^{\mu\nu\rho\sigma}, \quad (1.1)$$

where \mathcal{R} , $\mathcal{R}_{\mu\nu}$, and $\mathcal{R}_{\mu\nu\rho\sigma}$ are the n -dimensional scalar curvature, the Ricci tensor, and the Riemann curvature, respectively. This particular combination gives us several reasonable properties, such as ghost-free combinations [4], and a set of equations up to the second derivative in spite of the higher-curvature combinations. The theory is expected to have singularity-avoidance features in the context of gravitational collapses and/or cosmology. However, only a few studies so far have reported on the investigation of nonlinear dynamical features in Einstein-GB gravity (e.g., numerical studies on critical phenomena [5,6], black-hole formation in AdS [7,8]).

Our first investigative model concerns wormhole dynamics. A wormhole is a hypothetical object such as a short-cut tunnel connecting two points in space-time. The idea is frequently used in science fiction to allow for rapid interstellar travel, warp drives, and time machines. However, wormholes are also a theoretical research topic with a long history. (See a review, e.g., Visser [9] for earlier works; see also e.g., Lobo [10,11] for recent works.)

We are especially interested in the fate of a perturbed Ellis wormhole [12], whose behavior is well known in four-dimensional GR. The Ellis wormhole is constructed with a massless Klein-Gordon field whose kinetic term takes the sign opposite to normal, which was rediscovered by Morris and Thorne [13], who considered “traversable conditions” for human travel through wormholes in a response to Carl Sagan's idea for his novel *Contact*.

The first numerical simulation on its stability behavior was reported by one of the authors [14]. It shows that the

*hisaki.shinkai@oit.ac.jp
†takashi.torii@oit.ac.jp

Ellis wormhole is unstable against the injection of perturbed field to the throat, and the wormhole will be changed either to a black hole or to an expanding throat depending on the energy balance. These basic behaviors were repeatedly confirmed by other groups [15–18]. We will explain in more detail in Sec. III.

In this article, we present numerical evolutions of higher-dimensional wormholes with the GB terms. Wormhole studies in higher-dimensional space-time is not a new topic. We can find articles on the subject from the 1980s [19,20], and recent studies are including higher-curvature terms (see, e.g., Ref. [21], Refs. [22,23], and references therein). Most of the research mainly concerns the solutions and their energy conditions, but to our knowledge there is no general discussion on the nonlinear stability issues of the solutions (linear stability analysis can be found in Refs. [22,23]). Studies on wormholes in Einstein-GB gravity have long histories. Several solutions and their classifications are reported in Refs. [24,25], while their energy conditions are considered in Ref. [21]. Similar research is extended to Lovelock gravity [26], and also to the dilatonic GB system [22,23].

A couple of years ago, we constructed Ellis-type solutions in higher-dimensional GR and reported stability analysis using a linear perturbation method [27]. The solutions have at least one negative mode, which leads to the conclusion that all Ellis-type (static and spherically symmetric) wormholes in GR are linearly unstable [28]. The time scale of instability becomes shorter as n becomes large. Therefore, the confirmation of these predictions and the dynamical behavior with the GB terms are two main objectives in Sec. III.

Our second investigative model deals with colliding wave packets. Due to the nonlinear features of the theory, in GR, gravitational waves interact with themselves when they pass through each other. Considering a collision of plane gravitational waves is the simplest scenario of this nonlinear interaction problem (see Ref. [32] and references therein).

In fact, Penrose [33] pointed out that the future light cone of a plane wave is distorted as it passes through another plane wave. As one aspect of this global property, Szekeres [34] and Khan and Penrose [35] found exact solutions of colliding plane waves in flat space-time, which form a curvature singularity in their interacting region. Stewart *et al.* [36,37] performed numerical simulations in the framework of a $2+2$ decomposition of space-time and found that the expansion of the null geodesic will be negative after a collision of waves. Since these solutions assume a plane-symmetric space-time, this singularity does not have a horizon; it is a “naked” one.

Our attention to this problem focuses on the differences in the growth of curvature, especially the dependences on the dimension and the GB terms. We have found that we can compare the behaviors more easily when we place colliding matter rather than colliding gravitational waves.

Therefore, we prepare the model of colliding normal scalar packets in plane-symmetric space-time, and we show comparisons in Sec. IV.

The construction of this article is as follows: In Sec. II, we show the set of field equations in the form of a dual-null coordinate system and explain our numerical schemes. We then show the results of the evolutions of a perturbed wormhole in Sec. III, and the results of the collision of scalar plane pulses in Sec. IV. Section V provides a summary.

II. FIELD EQUATIONS AND NUMERICAL TECHNIQUE

A. Action

The Einstein-GB action in n -dimensional space-time $(\mathcal{M}, g_{\mu\nu})$ is described as

$$S = \int_{\mathcal{M}} d^n x \sqrt{-g} \left[\frac{1}{2\kappa^2} (\alpha_{\text{GR}} \mathcal{R} - 2\Lambda + \alpha_{\text{GB}} \mathcal{L}_{\text{GB}}) + \mathcal{L}_{\text{matter}} \right], \quad (2.1)$$

where \mathcal{L}_{GB} is the GB term [Eq. (1.1)], κ^2 is the n -dimensional gravitational constant, and $\mathcal{L}_{\text{matter}}$ is the matter Lagrangian. This action reproduces the standard n -dimensional Einstein gravity, if we set the coupling constant α_{GB} equal to zero. On the other hand, by setting $\alpha_{\text{GR}} = 0$, the system becomes pure GB gravity. In the actual simulations, we set $\alpha_{\text{GR}} = 1$, $\Lambda = 0$, $\kappa^2 = 1$ and change α_{GB} as a parameter while we write the set of equations with α_{GR} and Λ in this section in order to compare the terms with those from \mathcal{L}_{GB} .

The action (2.1) gives the gravitational equation as

$$\alpha_{\text{GR}} G_{\mu\nu} + g_{\mu\nu} \Lambda + \alpha_{\text{GB}} H_{\mu\nu} = \kappa^2 T_{\mu\nu}, \quad (2.2)$$

where

$$G_{\mu\nu} = \mathcal{R}_{\mu\nu} - \frac{1}{2} g_{\mu\nu} \mathcal{R}, \quad (2.3)$$

$$H_{\mu\nu} = 2(\mathcal{R} \mathcal{R}_{\mu\nu} - 2\mathcal{R}_{\mu\alpha} \mathcal{R}^{\alpha}_{\nu} - 2\mathcal{R}^{\alpha\beta} \mathcal{R}_{\mu\alpha\beta} + \mathcal{R}_{\mu}^{\alpha\beta\gamma} \mathcal{R}_{\nu\alpha\beta\gamma}) - \frac{1}{2} g_{\mu\nu} \mathcal{L}_{\text{GB}}, \quad (2.4)$$

$$T_{\mu\nu} = -2 \frac{\delta \mathcal{L}_{\text{matter}}}{\delta g^{\mu\nu}} + g_{\mu\nu} \mathcal{L}_{\text{matter}}. \quad (2.5)$$

B. Dual-null formulation

We use dual-null formulation for expressing space-time which has spherical symmetry (Sec. III) or planar symmetry (Sec. IV) [38]. The use of dual-null coordinates simplifies the treatment of horizon dynamics, enables us to approach close to large-curvature regions, and also clarifies radiation propagation in far regions. We implement

our dual-null evolution code which was used for four-dimensional GR [14] so as to follow higher-dimensional space-time with the GB terms.

We adopt the line element

$$ds^2 = -2e^{f(x^+, x^-)} dx^+ dx^- + r^2(x^+, x^-) \gamma_{ij} dz^i dz^j, \quad (2.6)$$

where the coordinates (x^+, x^-) are along the null propagation directions, and $\gamma_{ij} dx^i dx^j$ is the metric of the $(n-2)$ -dimensional unit constant-curvature space with $k = \pm 1, 0$.

For writing down the field equations, we introduce the variables

$$\Omega \equiv \frac{1}{r}, \quad (2.7)$$

$$\vartheta_{\pm} \equiv (n-2)\partial_{\pm} r, \quad (2.8)$$

$$\nu_{\pm} \equiv \partial_{\pm} f, \quad (2.9)$$

where $\partial_{\pm} \equiv \partial/\partial x^{\pm}$, and these are the conformal factor, expansions, and inaffinities, respectively.

The nonzero Einstein tensor components, then, are

$$\alpha_{\text{GR}} G_{++} = -\Omega(\partial_+ \vartheta_+ + \vartheta_+ \nu_+)(1 + 2\tilde{\alpha}\Omega^2 Z), \quad (2.10)$$

$$\alpha_{\text{GR}} G_{--} = -\Omega(\partial_- \vartheta_- + \vartheta_- \nu_-)(1 + 2\tilde{\alpha}\Omega^2 Z), \quad (2.11)$$

$$\begin{aligned} \alpha_{\text{GR}} G_{+-} = & \Omega \partial_- \vartheta_+ + \frac{(n-2)(n-3)\Omega^2}{2} \left[k e^{-f} + \frac{2}{(n-2)^2} \vartheta_+ \vartheta_- \right] \\ & + \tilde{\alpha} \left[\frac{(n-2)(n-5)}{2} k^2 \Omega^4 e^{-f} + 2\Omega^3 Z \partial_- \vartheta_+ + \frac{2(n-5)}{n-2} \Omega^4 Z \vartheta_+ \vartheta_- \right] - \Lambda e^{-f}, \end{aligned} \quad (2.12)$$

$$\begin{aligned} \alpha_{\text{GR}} G_{ij} = & \gamma_{ij} \left\{ e^f \left[\frac{\partial_{(+}\nu_-)}{\Omega^2} - \frac{2(n-3)}{(n-2)\Omega} \partial_{(-}\vartheta_+) - \frac{(n-3)(n-4)}{(n-2)^2} \vartheta_+ \vartheta_- \right] - \frac{(n-3)(n-4)k}{2} \right\} \\ & + \tilde{\alpha} \gamma_{ij} \left\{ 2e^f Z \left[\partial_{(+}\nu_-) - \frac{2(n-5)\Omega}{n-2} \partial_{(-}\vartheta_+) - \frac{(n-5)\Omega^2}{n-2} \vartheta_+ \vartheta_- \right] \right. \\ & + \frac{4e^{2f}}{(n-2)^2} [(\partial_+ \vartheta_+ + \nu_+ \vartheta_+)(\partial_- \vartheta_- + \nu_- \vartheta_-) - (\partial_{(-}\vartheta_+)^2] \\ & \left. + 2(n-5)Z^2 \Omega^2 - \frac{(n-2)(n-5)}{2} k^2 \Omega^2 \right\} + \Lambda r^2 \gamma_{ij}, \end{aligned} \quad (2.13)$$

where $\tilde{\alpha} = (n-3)(n-4)\alpha_{\text{GB}}$, $Z = k + W$, $W = \frac{2e^f}{(n-2)^2} \vartheta_+ \vartheta_-$, and we use the expression, $a_{(+}b_-) = \frac{1}{2}(a_+b_- + a_-b_+)$.

The set of dual-null field equations, then, becomes

$$\partial_+ \vartheta_+ = -\vartheta_+ \nu_+ - \frac{1}{\Omega A} \kappa^2 T_{++}, \quad (2.14)$$

$$\partial_- \vartheta_- = -\vartheta_- \nu_- - \frac{1}{\Omega A} \kappa^2 T_{--}, \quad (2.15)$$

$$\partial_- \vartheta_+ = \frac{1}{\Omega A} \left[-\frac{\alpha_{\text{GR}}(n-2)(n-3)}{2} \Omega^2 e^{-f} Z + e^{-f} \Lambda + \kappa^2 T_{+-} \right] - \frac{\tilde{\alpha}(n-2)(n-5)\Omega^3 e^{-f}}{2A} (k^2 + 2WZ), \quad (2.16)$$

and

$$\begin{aligned} \partial_+ \nu_- = & \alpha_{\text{GR}}(n-3) \frac{Z e^{-f} \Omega^2}{A} \left[-\frac{\alpha_{\text{GR}}(n-3)}{A} + \frac{(n-4)}{2} \right] + \frac{e^{-f} \Lambda}{A} \left[\frac{2\alpha_{\text{GR}}(n-3)}{(n-2)A} - 1 \right] + \frac{2(n-3)}{(n-2)A^2} \kappa^2 T_{+-} + \frac{\Omega^2 e^{-f}}{A} \kappa^2 T_{zz} \\ & + \tilde{\alpha}(n-5) \frac{\Omega^2 e^{-f}}{A^2} \left\{ -\alpha_{\text{GR}}(n-3)\Omega^2(k^2 + 2WZ + 2Z^2) - 2\tilde{\alpha}(n-5)\Omega^4(k^2 + 2WZ)Z + \frac{\Omega^2 A}{2} [(n-2)k^2 + 2WZ \right. \\ & \left. - 4Z^2] + \frac{4Z}{n-2} (\Lambda + e^f \kappa^2 T_{+-}) \right\} - \frac{4\tilde{\alpha}}{(n-2)^2} \frac{\Omega^2 e^f}{A} [(\partial_+ \vartheta_+ + \nu_+ \vartheta_+)(\partial_- \vartheta_- + \nu_- \vartheta_-) - (\partial_{(-}\vartheta_+)^2], \end{aligned} \quad (2.17)$$

where $A = \alpha_{\text{GR}} + 2\tilde{\alpha}\Omega^2 Z$. Note that $\partial_+ \vartheta_- = \partial_- \vartheta_+$ and $\partial_+ \nu_- = \partial_- \nu_+$.

C. Matter terms

We assume two scalar fields: the normal field $\psi(x^+, x^-)$ and the ghost field $\phi(x^+, x^-)$,

$$T_{\mu\nu} = T_{\mu\nu}^{\psi} + T_{\mu\nu}^{\phi}, \quad (2.18)$$

where

$$T_{\mu\nu}^{\psi} = \partial_{\mu}\psi\partial_{\nu}\psi - g_{\mu\nu} \left[\frac{1}{2}(\nabla\psi)^2 + V_{\psi}(\psi) \right], \quad (2.19)$$

$$T_{\mu\nu}^{\phi} = -\partial_{\mu}\phi\partial_{\nu}\phi - g_{\mu\nu} \left[-\frac{1}{2}(\nabla\phi)^2 + V_{\phi}(\phi) \right] \quad (2.20)$$

both obey the Klein-Gordon equations,

$$\square\psi = \frac{dV_{\psi}}{d\psi}, \quad \phi = \frac{dV_{\phi}}{d\phi}, \quad (2.21)$$

respectively. If we define the scalar momenta as

$$\pi_{\pm} \equiv r\partial_{\pm}\psi = \frac{1}{\Omega}\partial_{\pm}\psi, \quad (2.22)$$

$$p_{\pm} \equiv r\partial_{\pm}\phi = \frac{1}{\Omega}\partial_{\pm}\phi, \quad (2.23)$$

then the nonzero $T_{\mu\nu}$ components are

$$T_{++} = \Omega^2(\pi_+^2 - p_+^2), \quad (2.24)$$

$$T_{--} = \Omega^2(\pi_-^2 - p_-^2), \quad (2.25)$$

$$T_{+-} = T_{-+} = e^{-f}(V_{\psi} + V_{\phi}), \quad (2.26)$$

$$T_{z_i z_j} = \left[e^f(\pi_+\pi_- - p_+p_-) - \frac{1}{\Omega^2}(V_{\psi} + V_{\phi}) \right] \gamma_{ij}. \quad (2.27)$$

Equation (2.21) becomes

$$2\partial_+\pi_- = \frac{4-n}{n-2}\Omega\partial_+\pi_- - \Omega\partial_-\pi_+ - \frac{1}{e^f\Omega}\frac{dV_{\psi}}{d\psi}, \quad (2.28)$$

$$2\partial_-\pi_+ = \frac{4-n}{n-2}\Omega\partial_-\pi_+ - \Omega\partial_+\pi_- - \frac{1}{e^f\Omega}\frac{dV_{\psi}}{d\psi}, \quad (2.29)$$

$$2\partial_+p_- = \frac{4-n}{n-2}\Omega\partial_+p_- - \Omega\partial_-\pi_+ - \frac{1}{e^f\Omega}\frac{dV_{\phi}}{d\phi}, \quad (2.30)$$

$$2\partial_-\pi_+ = \frac{4-n}{n-2}\Omega\partial_-\pi_+ - \Omega\partial_+\pi_- - \frac{1}{e^f\Omega}\frac{dV_{\phi}}{d\phi}. \quad (2.31)$$

These equations complete the system.

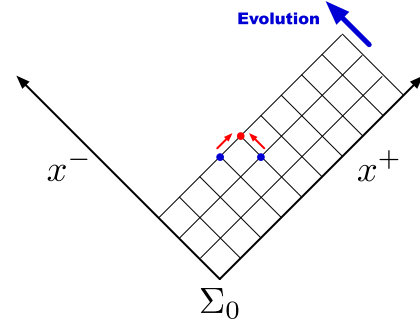


FIG. 1. Numerical grid structure. Initial data are given on null hypersurfaces Σ_{\pm} ($x^{\mp} = 0$, $x^{\pm} > 0$) and their intersection Σ_0 .

D. Numerical integration scheme

The basic idea of numerical integration is as follows: We prepare our numerical integration range as drawn in Fig. 1. We give initial data on a surface Σ_0 , where $x^+ = x^- = 0$, and the two null hypersurfaces Σ_{\pm} generated from it, where $x^{\mp} = 0$ and $x^{\pm} > 0$. Generally, the initial data have to be given as

$$(\Omega, f, \vartheta_{\pm}, \phi, \psi) \quad \text{on } \Sigma_0, \quad (2.32)$$

$$(\nu_{\pm}, p_{\pm}, \pi_{\pm}) \quad \text{on } \Sigma_{\pm}. \quad (2.33)$$

We then evolve the data $u = (\Omega, \vartheta_{\pm}, f, \nu_{\pm}, \phi, \psi, p_{\pm}, \pi_{\pm})$ on a constant- x^- slice to the next.

Due to the dual-null decomposition, the causal region of a grid is clear, and there are in-built accuracy checks: the integrability conditions or consistency conditions $\partial_-\partial_+u = \partial_+\partial_-u$. In order to update a point N (north), we have two routes from the points E (east) and W (west). The sets of equations (2.14)–(2.17) [with Eqs. (2.24)–(2.27)] and (2.28)–(2.31) give us the updates in the x^+ direction (from W to N) and in the x^- direction (from E to N) together with the consistency conditions. Note, however, that there are no equations for $\partial_+\nu_+$, $\partial_-\nu_-$, $\partial_{\pm}\pi_{\pm}$, and $\partial_{\pm}p_{\pm}$, so the consistency on these variables will be checked by other methods. More detailed procedures are given in Ref. [14].

As a virtue of the dual-null scheme, we can follow the wormhole throat or black-hole horizons easily. They are both trapping horizons, hypersurfaces where $\vartheta_+ = 0$ or $\vartheta_- = 0$ [40,41]. The region between $\vartheta_+ = 0$ and $\vartheta_- = 0$ is recognized as a trapped region if $\vartheta_+ = 0$ locates outer (x^+ direction), and if such a boundary runs null, we can say that a trapped region is a black hole [see Fig. 2(a)].

Another benefit is the singular-point excision technique. As we described, the causal region of each grid point in the dual-null scheme is apparent. When a grid point is inside a black-hole horizon and near to the singularity, we can exclude that point and grid points in its future null cone from further numerical computation.

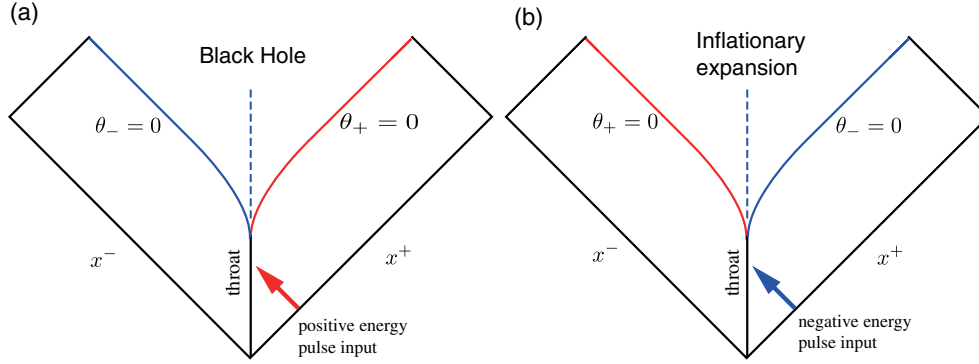


FIG. 2. Partial Penrose diagrams of the evolved space-time. Suppose we live in the right-side region and input a pulse to an Ellis wormhole in the middle of each diagram. The wormhole throat suffers a bifurcation of horizons and either (a) collapses to a black hole, or (b) explodes to form an inflationary universe, depending on whether the total input energy is positive or negative, respectively. This basic picture was first given by Ref. [14], and it holds for higher-dimensional GR, as will be shown in Fig. 3, while in the Einstein-GB gravity slight changes are observed, as will be shown in Fig. 4.

E. Initial data construction

For the preparation of initial data on Σ_0 ($x^+ = x^- = 0$) and on Σ_{\pm} ($x^{\mp} = 0, x^{\pm} > 0$), we integrate the set of equations (∂_+ equations, and ∂_- equations) from the center Σ_0 . When we consider static solutions, some additional consistency relations appear. These are

$$\vartheta_+ + \vartheta_- = 0, \quad (2.34)$$

$$\nu_+ + \nu_- = 0, \quad (2.35)$$

$$\pi_+ + \pi_- = 0, \quad (2.36)$$

$$p_+ + p_- = 0, \quad (2.37)$$

which are given from $(\partial_+ + \partial_-)\Omega = 0$, $(\partial_+ + \partial_-)f = 0$, $(\partial_+ + \partial_-)\psi = 0$, and $(\partial_+ + \partial_-)\phi = 0$, respectively, together with

$$e^f \vartheta_+ \nu_+ = -\frac{\alpha_{\text{GR}}(n-2)(n-3)}{2} \Omega^2 (k+W) + \Lambda + \kappa^2 (V_\psi + V_\phi) - \frac{\tilde{\alpha}(n-2)(n-5)\Omega^3}{2A} (k^2 + 2kW + 2W^2) - \frac{\Omega e^f}{A} \kappa^2 (\pi_+^2 - p_+^2), \quad (2.38)$$

$$e^f (\partial_+ + \partial_- + \nu_-) \vartheta_- = \frac{1}{\Omega A} \left[-\frac{\alpha_{\text{GR}}(n-2)(n-3)}{2} \Omega^2 (k+W) + \Lambda + \kappa^2 (V_\psi + V_\phi) \right] - \frac{\tilde{\alpha}(n-2)(n-5)\Omega^3}{2A} (k^2 + 2kW + 2W^2) - \frac{\Omega e^f}{A} \kappa^2 (\pi_-^2 - p_-^2), \quad (2.39)$$

which are given from $(\partial_+ + \partial_-)\vartheta_+ = 0$ and $(\partial_+ + \partial_-)\vartheta_- = 0$, respectively.

When we consider a static configuration, we have requirements on Σ_0 ; $\vartheta_+ = \vartheta_- = 0$ and $\nu_+ = \nu_- = 0$. We also have a constraint on the matter:

$$\Omega e^f \kappa^2 (\pi_+^2 - p_+^2) = \frac{1}{\Omega} \left[-\frac{\alpha_{\text{GR}}(n-2)(n-3)}{2} k \Omega^2 + \Lambda + \kappa^2 (V_\psi + V_\phi) \right] - \frac{\tilde{\alpha}(n-2)(n-5)}{2} k^2 \Omega^3, \quad (2.40)$$

which is derived from $\partial_+ \vartheta_{\pm} = -\partial_- \vartheta_{\pm}$, and this constraint will be concerned when we set π_{\pm}, p_{\pm} on Σ_0 .

F. Transformation from normal metric to dual-null metric

In Sec. III, we compare our numerically constructed initial data in a dual-null metric with the exact solution in a normal time-space metric. Such a transformation is given by the method below.

Suppose we identify a (t, r) metric

$$ds^2 = -F(t, r) dt^2 + \frac{1}{F(t, r)} dr^2 \quad (2.41)$$

$$= -F(t, r) (dt^2 - dr_*^2) \quad (2.42)$$

with a dual-null metric

$$ds^2 = -2e^{f(x^+, x^-)} dx^+ dx^-, \quad (2.43)$$

where a tortoise coordinate r_* is introduced as $\frac{dr}{dr_*} = F$. By identifying two coordinates as

$$x^+ = \frac{1}{\sqrt{2}}(t + r_*), \quad (2.44)$$

$$x^- = \frac{1}{\sqrt{2}}(t - r_*), \quad (2.45)$$

when we consider a static solution, the derivative of a function $G(t, r)$ in the x^+ direction is expressed as

$$\frac{d}{dx^+} G(t, r) = \frac{\partial r_*}{\partial x^+} \frac{dr}{dr_*} \frac{\partial G}{\partial r} = \frac{F}{\sqrt{2}} \frac{\partial G}{\partial r}. \quad (2.46)$$

Thus, the components in a (t, r) metric can be converted into a (x^+, x^-) metric.

G. Misner-Sharp mass

In order to evaluate the energy, we apply the Misner-Sharp mass in n -dimensional Einstein-GB gravity [21],

$$E_n = \frac{(n-2)A_{n-2}}{2\kappa_n^2 \Omega} \left\{ -\frac{2\Lambda}{(n-1)(n-2)\Omega^2} + k + \frac{2e^f}{(n-2)^2} \vartheta_+ \vartheta_- + \tilde{\alpha} \Omega^2 \left[k + \frac{2e^f}{(n-2)^2} \vartheta_+ \vartheta_- \right]^2 \right\}, \quad (2.47)$$

where A_{n-2} is the volume of the $(n-2)$ -dimensional unit constant-curvature space, i.e. $A_2 = \pi/\Omega^2$, $A_3 = 4\pi/(3\Omega^3)$, $A_4 = \pi^2/\Omega^4$, $A_5 = 8\pi^2/(15\Omega^5)$ for $k = 1$.

H. Kretschmann scalar

For evaluation of the magnitude of the curvature, we calculate the Kretschmann scalar in n dimensions:

$$\mathcal{I}^{(n)} = R^{ijkl} R_{ijkl}. \quad (2.48)$$

$\mathcal{I}^{(n)}$ is written as

$$\mathcal{I}^{(4)} = I_1 + 16I_2 + 4I_3, \quad (2.49)$$

$$\mathcal{I}^{(5)} = I_1 + 24I_2 + 12I_3, \quad (2.50)$$

$$\mathcal{I}^{(6)} = I_1 + 32I_2 + 20I_3 + 16I_4, \quad (2.51)$$

$$\mathcal{I}^{(7)} = I_1 + 40I_2 + 32I_3 + 32I_4, \quad (2.52)$$

where

$$I_1 = 4e^{2f} (\partial_+ \partial_- f)^2, \quad (2.53)$$

$$I_2 = \frac{e^{2f}}{r^2} \{ [(\partial_- f)(\partial_- r) + (\partial_- \partial_- r)] \times [(\partial_+ f)(\partial_+ r) + (\partial_+ \partial_+ r)] + (\partial_+ \partial_- r)^2 \}, \quad (2.54)$$

$$I_3 = \frac{[k + 2e^{2f}(\partial_- r)(\partial_+ r)]^2}{r^4}, \quad (2.55)$$

$$I_4 = \frac{[e^{2f}(\partial_+ r)(\partial_- r)]^2}{r^4}. \quad (2.56)$$

III. NUMERICAL EVOLUTIONS OF A PERTURBED WORMHOLE

In this section, we show the evolutions of the Ellis-type wormhole in higher-dimensional space-time both in GR and in the Einstein-GB gravity theories.

In four-dimensional GR, a wormhole is an unstable object. If it is perturbed, its throat suffers a bifurcation of horizons and either collapses to a black hole or explodes to form an inflationary universe, depending on whether the additional (perturbed) energy is positive or negative, respectively (see Fig. 2) [14].

The instability of the Ellis-type wormhole in n -dimensional GR is also shown using a linear perturbation method by us [27]. We showed that the solutions have at least one negative mode, which leads to the conclusion that all Ellis-type wormholes are linearly unstable. The time scale of instability becomes shorter as n becomes larger.

Therefore, the objectives of this section are to confirm the instability of higher-dimensional GR wormholes in the nonlinear regime and to investigate the behavior of Einstein-GB wormholes.

A. Wormholes in four-, five-, and six-dimensional GR

The solution shown in Ref. [27] is obtained in a spherically symmetric space-time ($k = +1$) with the metric

$$ds^2 = -F(t, r)e^{-2\delta(t, r)} dt^2 + F(t, r)^{-1} dr^2 + R(t, r)^2 \gamma_{ij} dz^i dz^j, \quad (3.1)$$

with a massless ghost scalar field ($V_\phi = 0$). In order to construct a static wormhole solution, the metric function is restricted as $F = F(r)$, $R = R(r)$, $\phi = \phi(r)$, and $\delta = 0$. By locating the throat of the wormhole at $r = 0$, and imposing the reflection symmetry at the throat, the solution of the field equations is obtained as

$$f \equiv 1, \quad R' = \sqrt{1 - \left(\frac{a_0}{R}\right)^{2(n-3)}}, \quad \phi = \frac{\sqrt{(n-2)(n-3)}}{\kappa} a_0^{n-3} \int \frac{1}{R(r)^{n-2}} dr, \quad (3.2)$$

where a_0 is the radius of the throat, i.e. $R(0) = a_0$, and a prime denotes a derivative with respect to r . We used this solution for confirmation of our numerical solution, using the method described in Sec. II F.

In order to construct the initial static data on Σ_{\pm} , we integrate x^+ equations [(2.14), (2.16) as $\partial_+ \vartheta_-$, (2.17), (2.28), and (2.30)] and x^- equations [(2.15), (2.16), (2.17) as $\partial_- \nu_+$, (2.29), and (2.31)] with the boundary values at the throat,

$$\Omega = \frac{1}{a_0}, \quad \vartheta_{\pm} = \nu_{\pm} = f = 0, \quad \phi = \phi_0, \quad (3.3)$$

where ϕ_0 is given by Eq. (3.2), and we set $p_{\pm} (< 0)$ from Eq. (2.40).

We find that numerical truncation error can quite easily destroy the static configuration, but it can be controlled with finer resolution. All the results below are shown after we have confirmed that the static solution of the wormhole is maintained during the evolution (in the x^- direction) in the range of discussion.

We add a perturbation to the static wormhole in the form of a Gaussian pulse, input from the right-hand universe. The perturbation is placed as a scalar-field momentum on the initial data Σ_+ as a form

$$\delta p_+ = c_1 \exp[-c_2(x^+ - c_3)^2] \quad (3.4)$$

for the ghost scalar field where c_1, c_2, c_3 are parameters, or

$$\delta \pi_+ = c_1 \exp[-c_2(x^+ - c_3)^2] \quad (3.5)$$

for the normal scalar field. The static wormhole solution is from the ghost field, and its total energy is zero. In this model, positive (negative) c_1 in the ghost field (3.4) indicates the addition of positive (negative) energy to the system, while $c_1 \neq 0$ in the normal field (3.5) indicates the addition of positive energy to the system. After we set this perturbation form, we re-solve the other variables on Σ_+ ; i.e., our perturbed initial data are all solutions of the system, and we can also add a perturbation beyond the linear level.

Figure 3 shows the results of four-, five-, and six-dimensional wormhole solutions with the above perturbations. The plots show the trajectories of the locations of vanishing expansions $\vartheta_{\pm} = 0$ in the (x^+, x^-) plane. We see that the wormhole throat is initially located where $\vartheta_+ = \vartheta_- = 0$, but after a small pulse hits it, the throat (or horizon) splits into two horizons ($\vartheta_+ = 0$ and $\vartheta_- = 0$), and they propagate in opposite directions, depending on the signature of the energy of the pulse.

If the location of $\vartheta_+ = 0$ is farther out (in the x^+ direction) than that of $\vartheta_- = 0$, then the region between $\vartheta_- = 0$ and $\vartheta_+ = 0$ is said to be *trapped*. If such a trapped surface runs null, then the region is judged to be a black hole. On the contrary, if $\vartheta_- = 0$ is farther out (in the

x^+ direction), then the region between $\vartheta_+ = 0$ and $\vartheta_- = 0$ can be judged as an expanding throat. These two differences are confirmed also by calculating the circumference radius (see Fig. 5, later).

The throat begins shrinking and turns into a black hole if we inject a positive-energy scalar flux (left panels in Figure 3), while the throat begins expanding if we input a negative-energy scalar flux (right panels). This fundamental feature is the same with those already reported in Ref. [14], and the fact that higher-dimensional cases show earlier bifurcation matches with the predicted behavior from the linear perturbation analysis in Ref. [27].

B. Wormholes in Einstein-GB gravity

We also evolved the perturbed wormhole initial data with the GB terms ($\alpha_{\text{GB}} \neq 0$) and studied their effects on the evolutions. We first prepared the static Ellis-type wormhole solution by solving equations on Σ_{\pm} numerically. We checked that the solution in $n = 4$ Einstein-GB gravity is identical with that in GR.

We then confirmed that the solution is static by evolving it without perturbation. We actually found that the evolutions with large $|\alpha_{\text{GB}}|$ are quite unstable numerically, and it is hard to keep its static configurations long enough. Therefore, we can present the results only for small- $|\alpha_{\text{GB}}|$ cases, for those we confirmed the static configuration is maintained for the range of discussion.

Figure 4 shows the cases of $n = 5$ and 6 Einstein-GB gravity with $\alpha_{\text{GB}} = +0.001$. The lines show the locations of horizons ($\vartheta_{\pm} = 0$). We change the amplitude of the perturbation, c_1 in Eq. (3.4), and find that for large c_1 , the throat turns into a black hole, while for small c_1 , the throat begins expanding. This statement will be clarified in Fig. 5.

Figure 5 shows the evolution behavior of the circumference radius of the throat. We plotted for the cases of Fig. 4. If the amplitude of the perturbation, c_1 , is above a particular value, then the throat begins shrinking, which indicates the formation of a black hole. The critical value of the parameter exists at $E \sim 1.0$ for $n = 5$ and at $E \sim 2.5$ for $n = 6$ in terms of the Misner-Sharp mass (2.47), which means the threshold is larger for $n = 6$. Since the energy of the injected pulse is always positive, the existence of the critical positive value for forming a black hole suggests that introducing the GB terms with $\alpha_{\text{GB}} > 0$ turns out to have a sort of “negative” energy. The larger threshold for forming a black hole in higher dimensions also indicates that such effects become stronger in higher dimensions.

For quantitative comparisons, we prepared Table I, in which we list how the initial (positive-energy) perturbation, ΔE , results in a black hole (if it is formed). We evaluated the Misner-Sharp mass (2.47) at the end of the grid, $x^+ = 5$, and measured the horizon coordinate, x_H^- where the outgoing trapping horizon, $\vartheta_+ = 0$, propagates at null. We see that in higher n , x_H^- is smaller, which indicates the early formation of a black hole due to the large instability.

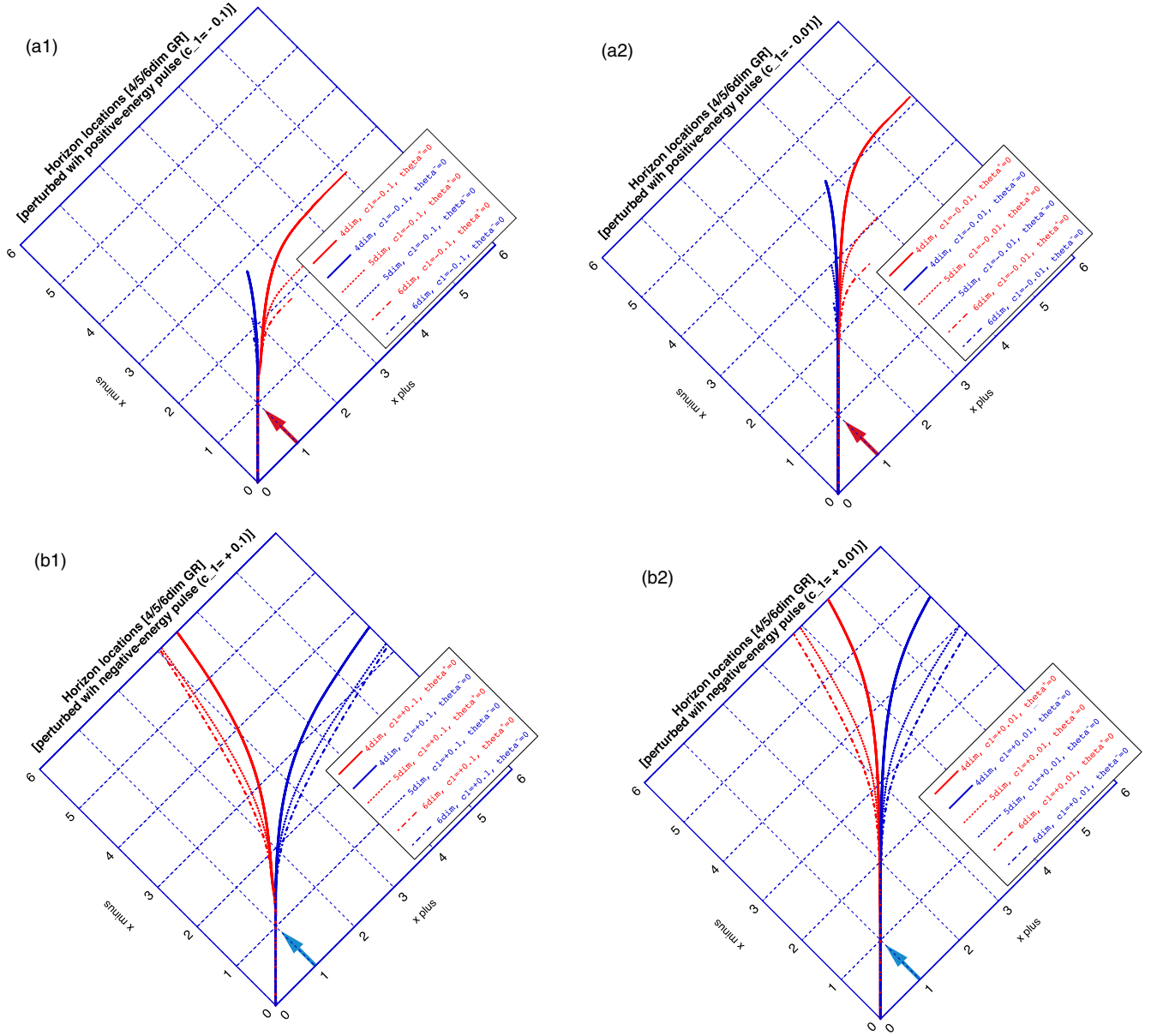


FIG. 3. Evolutions of a perturbed wormhole in four-, five-, and six-dimensional GR ($\alpha_{\text{GB}} = 0$). Locations of the horizons [where the expansions are $\vartheta_+ = 0$ (red lines) and $\vartheta_- = 0$ (blue lines)] are plotted as a function of (x^+, x^-) . Figures (a1) and (a2) are the results of the injection of a positive-energy scalar pulse which hits the throat at $x^+ = x^- = 1$, while Figures (b1) and (b2) are those of a negative-energy pulse. Arrows indicate the trajectories of pulses. The pulse parameters are $c_1 = -0.1$ for (a1), $c_1 = 0.1$ for (b1), $c_1 = -0.01$ for (a2), and $c_1 = 0.01$ for (b2). We also set $c_2 = 3$ and $c_3 = 1$, which means that the pulse hits the wormhole throat at $x^+ = x^- = 1$. The throat begins turning into a black hole if we input positive-energy scalar flux (upper panels), while the throat expands if we input negative-energy scalar flux (lower panels). This is what we expected from Fig. 2. We also see that the bifurcation of the throat appears earlier for higher dimensions, which suggests larger instability. The figures should be symmetric, but the large curvature stops numerical evolution just after a black hole is formed, so that the plots in the left panels are terminated in the middle of x^- .

Interestingly, the final mass of the black hole, E_f , depends only on the dimension n and α_{GB} , and does not depend on the injected energy, ΔE . The black-hole mass, E_f , is supposed to be a critically formed minimum mass of the black hole, and such an existence of the minimum mass (or threshold) was the same with those in the four-dimensional GR cases [14]. This threshold is larger for large α_{GB} . The

listed cases are fixed by the amplitude, c_1 , of the injected perturbation, but if we check the ratio E_f/E_i , then we see that the final mass of the black hole becomes smaller when α_{GB} is larger. Both suggest that the GB terms work for avoiding the appearance of a black hole (or singularity).

One more interesting finding is the critical case. When we tune the perturbation amplitude c_1 close to the critical

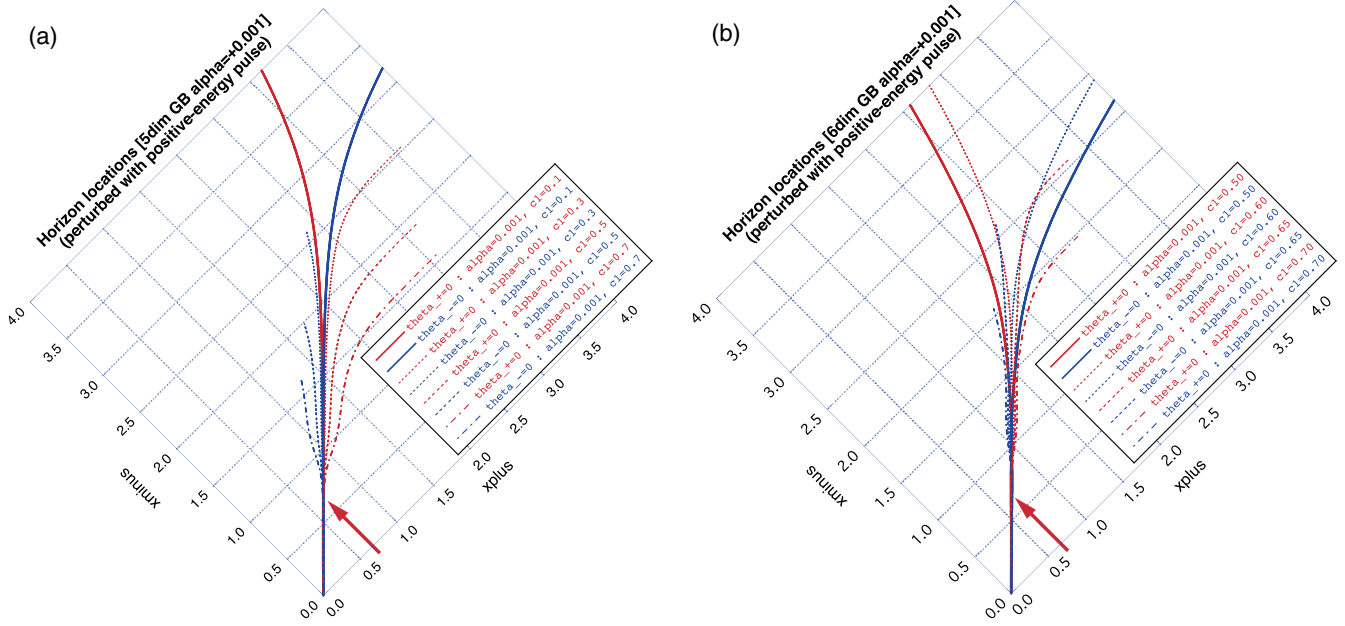


FIG. 4. Evolutions of a perturbed wormhole in Einstein-GB gravity with $\alpha_{\text{GB}} = +0.001$. The left and right panels show the cases of five- and six-dimensional space-time, respectively. Locations of the horizons [where the expansions are $\vartheta_{\pm} = 0$ (red lines) and $\vartheta_{-} = 0$ (blue lines)] are plotted as a function of (x^{+}, x^{-}) for several amplitudes of the perturbation (3.4) with $c_1 = 0.3, 0.5, 0.7$ for $n = 5$, and $c_1 = 0.5, 0.6, 0.65, 0.7$ for $n = 6$. The other parameters of the injections are $c_2 = 16$ and $c_3 = 0.7$. Arrows indicate the trajectories of pulses. We see that for large c_1 , the throat turns into a black hole, while for small c_1 , the throat begins expanding, which is different from GR cases.

value, as we show in Fig. 6, we find that the throat (double trapping horizon, $\vartheta_{\pm} = 0$) bifurcates to two trapping horizons ($\vartheta_{+} = 0$ and $\vartheta_{-} = 0$), and they remain at a quasi-constant radius, and shortly after that they propagate

outward. That is, the wormhole first changes to a *temporal* trapped region, and then decides its fate towards either a black hole or an expanding throat. Actually, the circumference radius of the throat in this critical case takes the

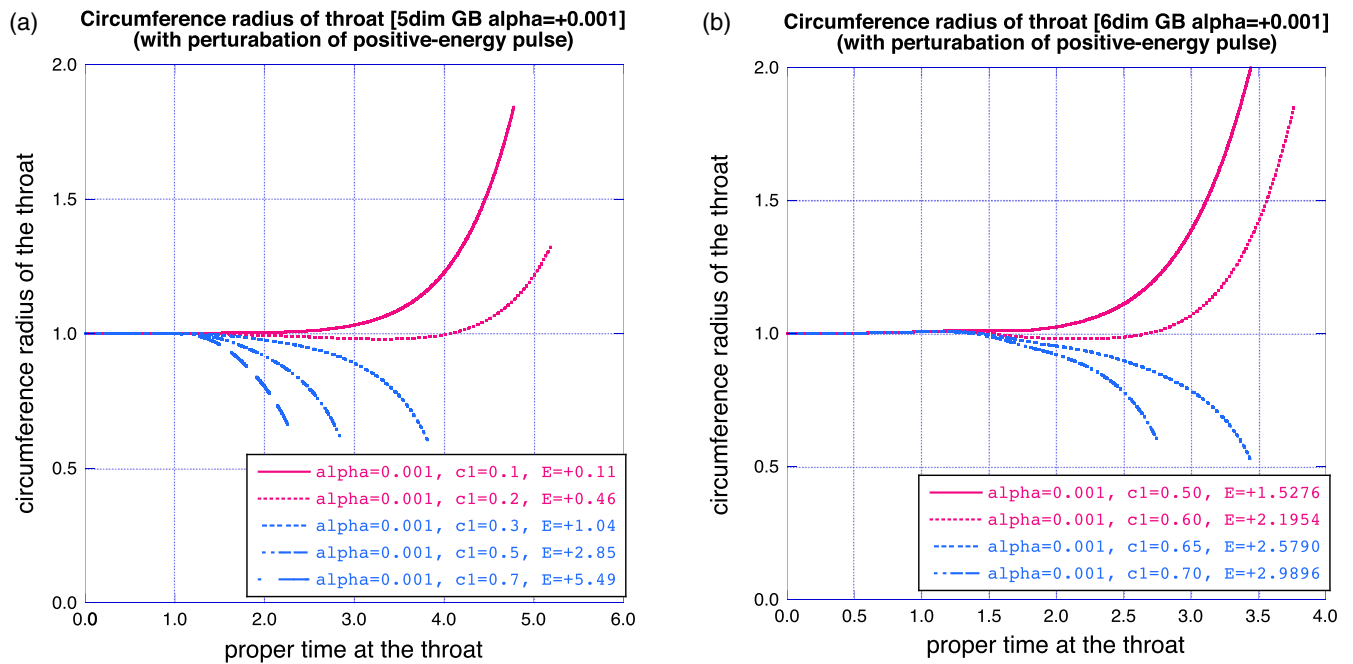


FIG. 5. The behavior of the circumference radius of the throat for the cases of Fig. 4. Panel (a) shows the cases of five-dimensional space-time, while (b) gives the cases of six-dimensional space-time. We see that if the amplitude of the perturbation, c_1 , is above a particular value, the throat begin shrinking, which indicates the formation of a black hole. This critical value is expressed with the Misner-Sharp mass (2.47), and we find that the magnitude is larger for $n = 6$.

TABLE I. Injected perturbation and the final black-hole structure (when it is formed). Initial Misner-Sharp energy ΔE , Eq. (2.47), is the additional energy due to the injected part. The amplitude c_1 in Eq. (3.5) is listed, while we set $c_2 = 16$ and $c_3 = 0.7$ for all cases. The total energies, E_i and E_f , are evaluated at $x^+ = 5$, and E_f is regarded as the mass of the black hole (when it is formed). The horizon coordinate x_H^- is evaluated where the $\vartheta_+ = 0$ trapping horizon becomes null.

n	α_{GB}	Injected field			Initial		Final BH		
		Field	c_1	$\Delta E/a_0$	E_i/a_0	E_f/a_0	x_H^-/a_0		
4	0	π_+	+0.25	+0.03	0.88	3.14	2.94		
4	0	π_+	+0.50	+0.10	0.95	3.14	2.09		
5	0	π_+	+0.25	+0.15	0.52	6.28	2.26		
5	0	π_+	+0.50	+0.61	0.97	6.28	1.66		
6	0	π_+	+0.25	+0.38	0.50	9.87	1.92		
6	0	π_+	+0.50	+1.50	1.63	9.87	1.46		
5	0.001	π_+	+0.25	+0.15	0.53	6.30	2.67		
5	0.001	π_+	+0.50	+0.61	0.98	6.30	1.72		
5	0.001	π_+	+1.00	+2.23	2.61	6.30	0.98		
5	0.01	π_+	+0.50	+0.59	1.02			noBH	
5	0.01	π_+	+0.75	+1.31	1.74	6.41	1.92		
5	0.01	π_+	+1.00	+2.21	2.65	6.41	1.19		
6	0.001	π_+	+0.50	+1.53	1.46			noBH	
6	0.001	π_+	+0.75	+3.42	3.36	9.93	1.34		
6	0.001	π_+	+1.00	+6.07	6.60	9.93	1.00		
6	0.01	π_+	+1.00	+6.90	5.00			noBH	
6	0.01	π_+	+1.50	+8.78	8.15			noBH	

value between the red lines and blue lines in Fig. 5; i.e., it remains almost constant but oscillates slightly when it is forming a *temporal* trapped region. Since the final two

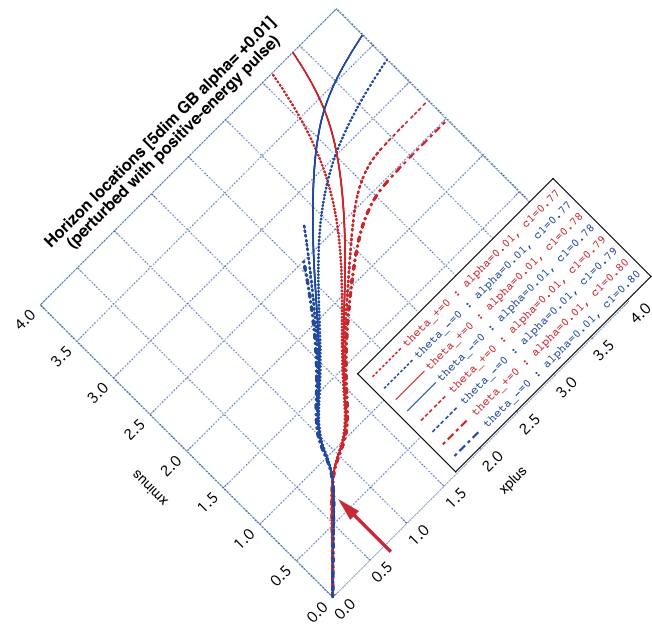


FIG. 6. The evolutions of the wormhole in the Einstein-GB theory (five-dimensional, $\alpha_{\text{GB}} = +0.01$). The locations of the horizons are plotted. When the amplitude of the perturbation, c_1 , is close to the critical value for the fate of the wormhole (either to expansion or to a black hole), a temporal trapped region with a constant radius appears. This behavior also suggests that the existence of such a trapped surface is not a necessary condition for forming a black hole in the Einstein-GB theory.

objects are totally different and there is no static configuration between them, we guess that this is the first-order transition.

This critical behavior also suggests us that the existence of such a trapped region is not a necessary condition for forming a black hole in this model. We do not know if such an observation is general in the presence of the GB terms, or if this is only due to the effect of the ghost field. We, however, note that, in Einstein-GB gravity, a couple of examples of the differences (from GR) in causality and energy conditions have been reported (e.g., Refs. [21,42]). Therefore, this new finding might not be surprising.

IV. NUMERICAL EVOLUTIONS OF THE COLLISION OF SCALAR PULSES

In this section, we show our results of the collision of massless scalar pulses in plane-symmetric space-time. There are several exact solutions of the colliding plane waves, which produce curvature singularity after their collisions (see, e.g., Ref. [32] and references therein). We prepare a similar situation in our code and examine such a strong curvature effect in higher-dimensional GR and in Einstein-GB gravity. We first note that in the construction of exact solutions, the wave fronts are assumed to be a step function, while in our simulations the wave fronts are a continuous function.

We put a perturbed normal scalar field (ψ) in the flat background on the initial surfaces and evolve it. The space-time is assumed to be plane symmetric ($k = 0$ in Sec. II), and we do not consider the ghost scalar field (ϕ) in this

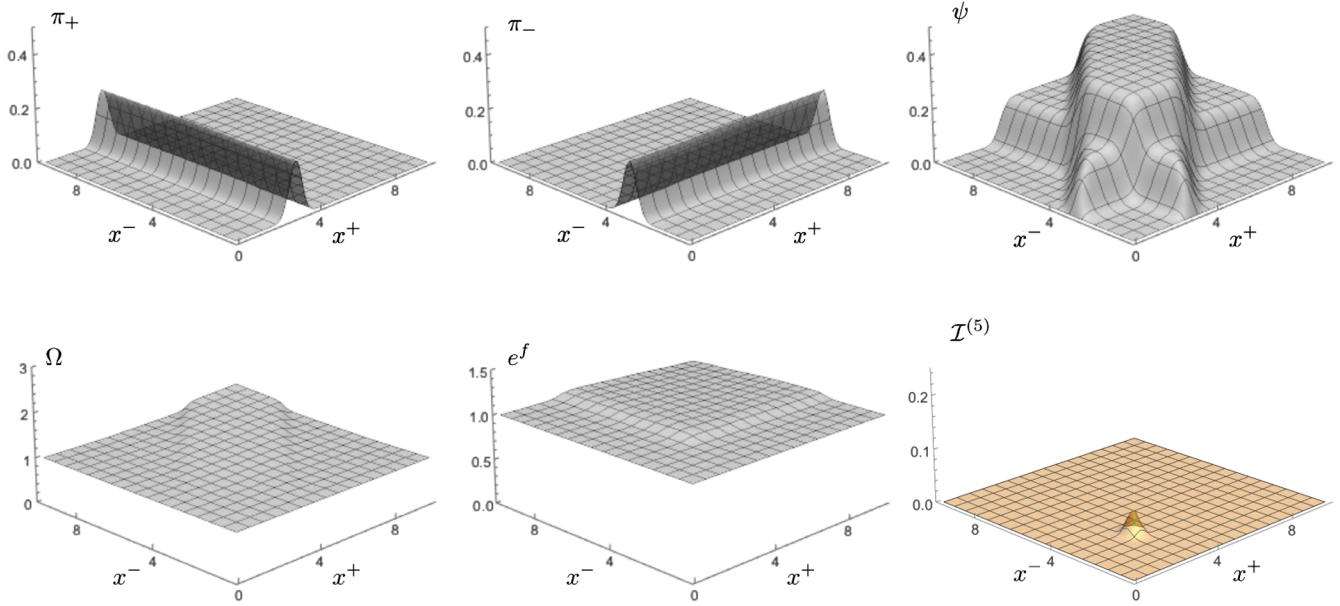
section. The initial scalar field is set as $\psi = 0$ and has momentum

$$\begin{cases} \pi_+ = a \exp(-b(x^+/\sqrt{2} - c)^2) \\ \pi_- = 0 \end{cases} \text{ on } \Sigma_+, \quad (4.1)$$

$$\begin{cases} \pi_+ = 0 \\ \pi_- = a \exp(-b(x^-/\sqrt{2} - c)^2) \end{cases} \text{ on } \Sigma_-, \quad (4.2)$$

where a, b, c are parameters.

(a) small amplitude case



(b) large amplitude case

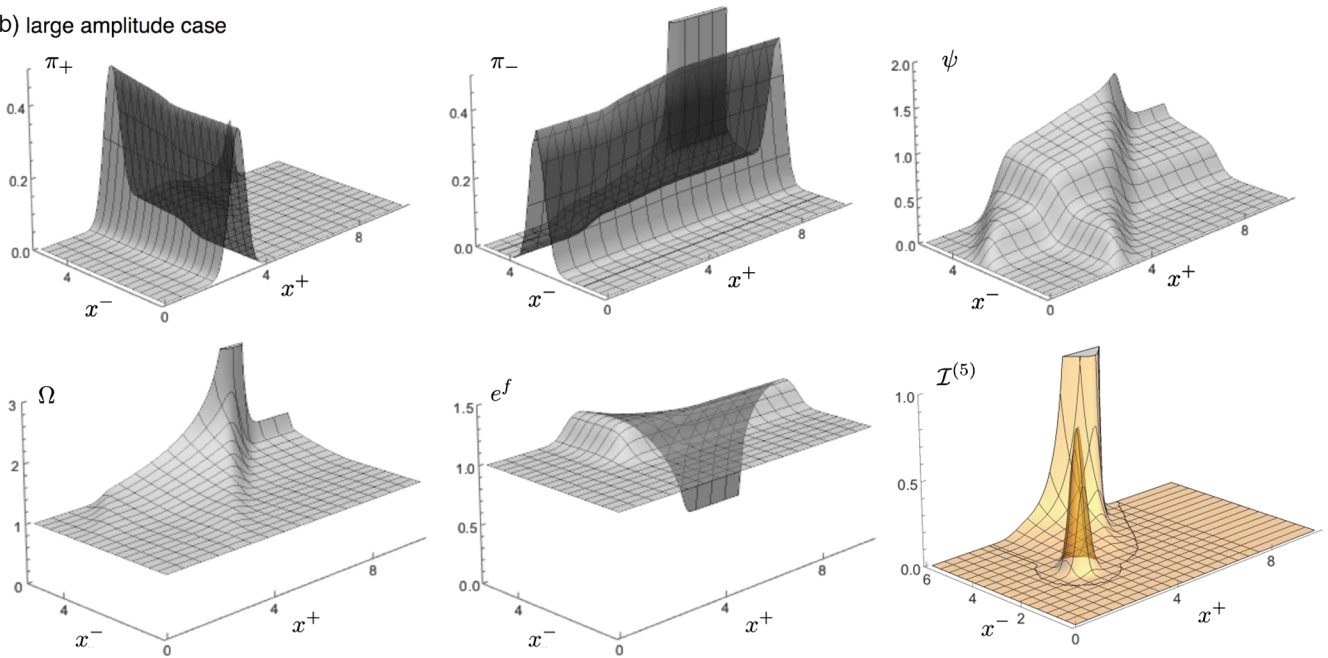
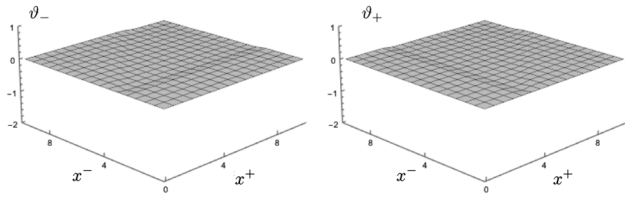


FIG. 7. Evolutions of colliding two scalar pulses in five-dimensional GR: (a) the small-amplitude case [$a = 0.2$ in Eqs. (4.1) and (4.2)], and (b) the large-amplitude case ($a = 0.4$). The scalar momentum π_{\pm} , scalar field ψ , the conformal factor Ω , metric function e^f , and the Kretschmann scalar $\mathcal{I}^{(5)}$ are plotted in the (x^+, x^-) coordinates. Initial data were set at both $\Sigma_-(x^+ = 0, x^- > 0)$ and $\Sigma_+(x^+ > 0, x^- = 0)$ and evolved. For small pulses, we see that they just cross, and space-time turns back toward flat again, while for large pulses, we see that non-linear curvature evolution appears after the collision of pulses. The latter behavior is similar to the exact solutions of the plane-wave collision.

(a) small amplitude case



(b) large amplitude case

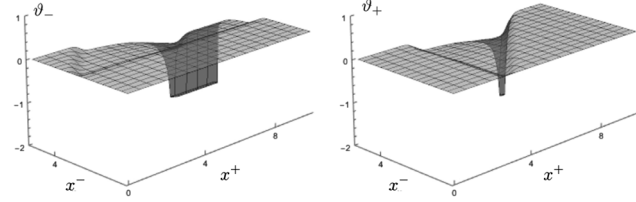


FIG. 8. The expansions ϑ_{\pm} for the evolutions shown in Fig. 7. (a) Small-amplitude case ($a = 0.2$). (b) Large-amplitude case ($a = 0.4$).

A. Evolutions in GR

The two typical evolutions are shown in Fig. 7. We plot the behaviors of the scalar field and the Kretschmann scalar, $\mathcal{I}^{(5)}$, for five-dimensional GR. We set $a = 0.2$ and 0.4 , and $b = 10$, $c = 2$ for these plots. For small pulses [Fig. 7(a)], we see that two pulses just pass through each other, and the curvature $\mathcal{I}^{(5)}$ turns back to flat again. On the contrary, for large pulses [Fig. 7(b)], the nonlinear curvature evolution appears after the collision of pulses. The latter behavior is similar to the exact solutions of the plane-wave collision (see, e.g., figures in Ref. [43]). We actually find that in all blow-up regions, both expansions are $\vartheta_{\pm} < 0$ (Fig. 8). In four-dimensional plane-symmetric space-time, if the curvature blows up, then it means the appearance of a naked singularity, since there is no chance to form a horizon. However, in higher dimensions, we expect such a blow-up will be hidden in a horizon, as the expansions suggest.

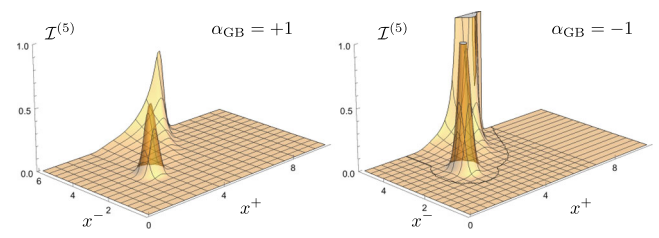
B. Evolutions in Einstein-GB

We also evolved the same initial data by the set of evolution equations with nonzero α_{GB} .

Figure 9(a) displays the Kretschmann scalar, $\mathcal{I}^{(5)}$, for both $\alpha_{\text{GB}} = +1$ and $\alpha_{\text{GB}} = -1$ cases for the same initial data with the large-amplitude case ($a = 0.4$) in Fig. 7(b). We see that the local peak of $\mathcal{I}^{(5)}$ at the collision of two pulses (at $x^+ = x^- = 2\sqrt{2}$) is smaller (larger) when $\alpha_{\text{GB}} > 0$ ($\alpha_{\text{GB}} < 0$) than that in GR. This result indicates that introducing the GB terms (in the way of the normal higher-curvature correction, $\alpha_{\text{GB}} > 0$) will work for reducing the growth of the local curvature.

In Fig. 9(b), we plot the “evolution” behavior of the Kretschmann scalar, $\mathcal{I}^{(5)}$, at the origin ($x^+ = x^-$) where

(a) large amplitude case, Gauss-Bonnet gravity



(b)

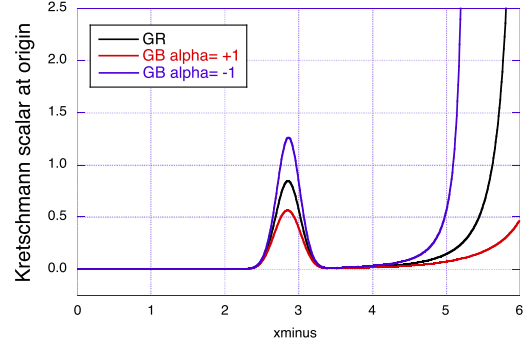


FIG. 9. (a) Kretschmann scalar, $\mathcal{I}^{(5)}$, of the evolutions of colliding two scalar pulses in five-dimensional Einstein-GB gravity with $\alpha_{\text{GB}} = \pm 1$. The initial data are the same with the large-amplitude case in Fig. 7(b). We see that the local peak of $\mathcal{I}^{(5)}$ at the collision of two pulses (at $x^+ = x^- = 2\sqrt{2}$) is smaller (larger) when $\alpha_{\text{GB}} > 1$ ($\alpha_{\text{GB}} < 1$). (b) Kretschmann scalar, $\mathcal{I}^{(5)}$, at the origin ($x^+ = x^-$) of these evolutions, together with one with $\alpha_{\text{GB}} = 0$ (i.e., GR).

two pulses collide. At later times, we see that the curvature will diverge for all the cases (GR and Einstein-GB) due to the large amplitude of the initial pulses, but these growing behaviors are again ordered by α_{GB} . Supposing that the curvature singularity will be formed at the final phase of this evolution (analogues to the plane-wave collision), then we can say that introducing the GB terms cannot stop the formation of the singularity, but it will shift its appearance later if $\alpha_{\text{GB}} > 0$.

Figure 10 shows the magnitude of the Kretschmann scalar, $\mathcal{I}^{(n)}$, at the moment of the collision of scalar pulses (at the first peak of $\mathcal{I}^{(n)}$). We plot the cases $\alpha_{\text{GB}} = 0, \pm 0.1, \pm 0.5, \pm 1.0$ and the dimensions $n = 4, 5, 6$, and 7 . We see that for $n = 4$, all three cases have the same magnitude, which is consistent with the fact that the GB correction does not appear at $n = 4$. For larger dimensions, the magnitude becomes lower. We also find that introducing positive α_{GB} (i.e., the normal higher-curvature correction) reduces its magnitude.

In summary, the collision of scalar pulses will produce curvature singularity if its initial amplitude is large enough, but its appearance will be delayed in higher dimensions and/or with the GB terms with $\alpha_{\text{GB}} > 0$.

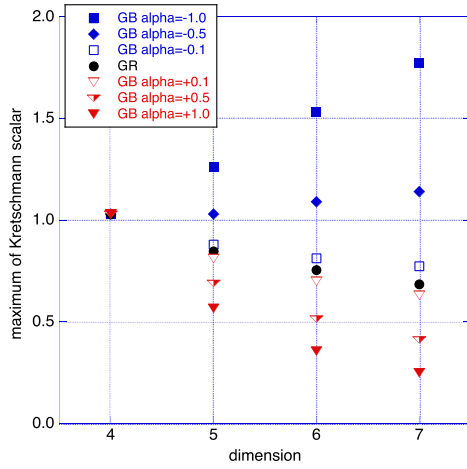


FIG. 10. The Kretschmann scalar, $\mathcal{I}^{(n)}$, at the moment of the collision of scalar pulses (at $x^+ = x^- = 2\sqrt{2}$). We plot for the models with $\alpha_{\text{GB}} = 0, \pm 0.1, \pm 0.5, \pm 1.0$ and for the dimensions $n = 4, 5, 6, 7$. For larger dimensions, the magnitude becomes lower in GR. We also find that introducing positive α_{GB} (i.e., the normal higher-curvature correction) reduces its magnitude.

V. SUMMARY AND DISCUSSIONS

The Einstein-GB gravity theory is one of the plausible candidates which describes the early Universe, but so far little is known of its nonlinear dynamical behaviors. We numerically investigated the dynamics in higher-dimensional space-time with and without the GB terms. We prepared a code for solving the full set of evolution equations in the spherically symmetric or planar symmetric space-time using the dual-null formulation, and we showed the dynamical features on two models, the fate of the perturbed wormhole and the collision of scalar pulses.

For wormhole dynamics, we monitored the throat structure of the static wormhole by injecting a perturbation to it. We confirmed the instability of the Ellis-type wormhole in higher dimensions, which was predicted from the linear analysis before. We also find that the fate of the

wormhole (to either a black hole or expanding throat) is determined by the signature of the total energy in GR which has the same features as those in four-dimensional cases. In Einstein-GB gravity, however, we observed that the threshold of the energy which makes a wormhole to a black hole is larger for the GB correction with the normal sign of the coupling constant ($\alpha_{\text{GB}} > 0$), and also larger for higher-dimensional cases. These facts indicate that adding the GB terms has similar effects to reducing the total energy of the system.

For scalar pulses' collision, we observed that curvature (Kretschmann scalar) evolves more mildly in the presence of the normal GB terms ($\alpha_{\text{GB}} > 0$) and in higher-dimensional space-time. The appearance of the singularity is inevitable in our model, but the basic feature is matched with the expected effect of the cosmologists; i.e., the avoidance (or lower possibility) of the appearance of the singularity.

Both models suggest consistent features: the chances of the appearance of a singularity or black hole will be reduced in higher-dimensional space-time and/or in the presence of the GB terms. As is shown in other models (e.g., Refs. [44,45]), in higher-dimensional GR, the chance of appearances of naked singularities is suppressed compared to the four-dimensional GR cases. This is suggested by the existence of many freedoms in gravity, which suppresses the growth of curvature and makes the formation of horizons less eccentric. The introduction of the GB terms seems to work for this direction.

We hope that these results will be used as a guiding principle for understanding the fundamental dynamical features of the Einstein-GB gravity.

ACKNOWLEDGMENTS

This work was supported in part by the Grant-in-Aid for the Scientific Research Fund of the JSPS (C) No. 25400277, and also by MEXT KAKENHI Grants No. 17H06357 and No. 17H06358.

-
- [1] D. Lovelock, *J. Math. Phys. (N.Y.)* **12**, 498 (1971).
 - [2] D.J. Gross and E. Witten, *Nucl. Phys.* **B277**, 1 (1986); D.J. Gross and J.H. Sloan, *Nucl. Phys.* **B291**, 41 (1987).
 - [3] R.R. Metsaev and A.A. Tseytlin, *Phys. Lett. B* **191**, 354 (1987); *Nucl. Phys.* **B293**, 385 (1987).
 - [4] B. Zwiebach, *Phys. Lett.* **156B**, 315 (1985); B. Zumino, *Phys. Rep.* **137**, 109 (1986).
 - [5] S. Golod and T. Piran, *Phys. Rev. D* **85**, 104015 (2012).
 - [6] N. Deppe, C. D. Leonard, T. Taves, G. Kunstatter, and R. B. Mann, *Phys. Rev. D* **86**, 104011 (2012).
 - [7] N. Deppe, A. Kolly, A. R. Frey, and G. Kunstatter, *Phys. Rev. Lett.* **114**, 071102 (2015).
 - [8] N. Deppe, A. Kolly, A. R. Frey, and G. Kunstatter, *J. High Energy Phys.* **10** (2016) 087.
 - [9] M. Visser, *Lorentzian Wormholes* (AIP Press, New York, 1995).
 - [10] F. S. N. Lobo, in *Classical and Quantum Gravity Research* (Nova Science Publishers, London, 2008).
 - [11] *Wormholes, Warp Drives and Energy Conditions*, edited by F. S. N. Lobo (Springer, New York, 2017).
 - [12] H. G. Ellis, *J. Math. Phys. (N.Y.)* **14**, 104 (1973).

- [13] M. S. Morris and K. S. Thorne, *Am. J. Phys.* **56**, 395 (1988).
- [14] H. Shinkai and S. A. Hayward, *Phys. Rev. D* **66**, 044005 (2002).
- [15] A. Doroshkevich, J. Hansen, I. Novikov, and A. Shatskiy, *Int. J. Mod. Phys. D* **18**, 1665 (2009).
- [16] J. A. Gonzalez, F. S. Guzman, and O. Sarbach, *Classical Quantum Gravity* **26**, 015010 (2009).
- [17] J. A. Gonzalez, F. S. Guzman, and O. Sarbach, *Classical Quantum Gravity* **26**, 015011 (2009).
- [18] J. A. Gonzalez, F. S. Guzman, and O. Sarbach, *Phys. Rev. D* **80**, 024023 (2009).
- [19] A. Chodos and S. Detweiler, *Gen. Relativ. Gravit.* **14**, 879 (1982).
- [20] G. Clément, *Gen. Relativ. Gravit.* **16**, 131 (1984).
- [21] H. Maeda and M. Nozawa, *Phys. Rev. D* **78**, 024005 (2008).
- [22] P. Kanti, B. Kleihaus, and J. Kunz, *Phys. Rev. Lett.* **107**, 271101 (2011).
- [23] P. Kanti, B. Kleihaus, and J. Kunz, *Phys. Rev. D* **85**, 044007 (2012).
- [24] B. Bhawal and S. Kar, *Phys. Rev. D* **46**, 2464 (1992).
- [25] G. Dotti, J. Oliva, and R. Troncoso, *Phys. Rev. D* **76**, 064038 (2007).
- [26] M. H. Dehghani and Z. Dayyani, *Phys. Rev. D* **79**, 064010 (2009).
- [27] T. Torii and H. Shinkai, *Phys. Rev. D* **88**, 064027 (2013).
- [28] Recent studies [29–31] of rotating Ellis-type wormholes show that this unstable mode is no longer present.
- [29] T. Matos and D. Núñez, *Classical Quantum Gravity* **23**, 4485 (2006).
- [30] V. Dzhunushaliev, V. Folomeev, B. Kleihaus, J. Kunz, and E. Radu, *Phys. Rev. D* **88**, 124028 (2013).
- [31] B. Kleihaus and J. Kunz, *Phys. Rev. D* **90**, 121503(R) (2014).
- [32] J. B. Griffiths, *Colliding Plane Waves in General Relativity* (Clarendon Press, Oxford, 1991) [Available also from Dover, New York, 2016].
- [33] R. Penrose, *Phys. Rev. Lett.* **14**, 57 (1965); *Rev. Mod. Phys.* **37**, 215 (1965).
- [34] P. Szekeres, *Nature (London)* **228**, 1183 (1970); *J. Math. Phys. (N.Y.)* **13**, 286 (1972).
- [35] V. A. Khan and R. Penrose, *Nature (London)* **229**, 185 (1971).
- [36] J. M. Stewart and H. Friedrich, *Proc. R. Soc. A* **384**, 427 (1982).
- [37] R. W. Corkill and J. M. Stewart, *Proc. R. Soc. A* **386**, 373 (1983).
- [38] We formulated $n + 1$ decomposition of the Einstein-GB field equations in Ref. [39], but we decided to apply the dual-null formulation in this study, since there are many advantages, as we wrote in the text.
- [39] T. Torii and H. Shinkai, *Phys. Rev. D* **78**, 084037 (2008).
- [40] S. A. Hayward, *Phys. Rev. D* **49**, 6467 (1994).
- [41] S. A. Hayward, *Classical Quantum Gravity* **15**, 3147 (1998).
- [42] K. Izumi, *Phys. Rev. D* **90**, 044037 (2014).
- [43] R. A. Matzner and F. J. Tipler, *Phys. Rev. D* **29**, 1575 (1984).
- [44] Y. Yamada and H. Shinkai, *Classical Quantum Gravity* **27**, 045012 (2010).
- [45] Y. Yamada and H. Shinkai, *Phys. Rev. D* **83**, 064006 (2011).